Journal of Zhejiang University-SCIENCE A (Applied Physics & Engineering) 2023 24(4):303-318
www.jzus.zju.edu.cn; www.springer.com/journal/11582
E-mail: jzus_a@zju.edu.cn

Research Article

https://doi.org/10.1631/jzus.A2200226

Check for updates

Effect of morphological gene mutation and decay on energy dissipation behaviour of granular soils

Wei XIONG[1], Qi-min ZHANG[1], Jian-feng WANG[1,2]✉

[1]*Department of Architecture and Civil Engineering, City University of Hong Kong, Hong Kong, China*
[2]*Shenzhen Research Institute of City University of Hong Kong, Shenzhen 518057, China*

Abstract: In this paper, the X-ray micro-computed tomography (X-ray μCT), spherical harmonical-based principal component analysis (SH-PCA), and discrete element method (DEM) were incorporated to generate virtual samples with morphological gene mutation at different length scales. All samples were subjected to axial compression and constant confining stress. The effects of multiscale particle morphology on the stress-strain and energy storage/dissipation responses of granular soils were investigated. It is found that: (a) the effects of particle morphology on the initial stiffness, stress-strain, volumetric strain, and frictional energy dissipation behaviours are more pronounced for looser samples than for denser ones; (b) among different length scales, the particle morphology at the local roundness-level outperforms the one at the general form-level in dictating the macro-scale responses of granular soils; (c) the energy dissipation of a granular assemblage is a result of competition between particle morphology and initial void ratio.

Key words: X-ray micro-computed tomography (X-ray μCT); Spherical harmonic analysis (SHA); Discrete element method (DEM); Morphological gene mutation; Energy dissipation

1 Introduction

Granular soil is ubiquitous in nature and widely utilized in geotechnical engineering practice. The typical characteristics of such materials, discontinuity and heterogeneity, usually lead to complex mechanical responses under triaxial shear. Within a granular assemblage, particles can rotate, translate, and even break during the whole shearing process, leading to the loss and gain of interparticle contacts (Fonseca et al., 2013; Cheng and Wang, 2018a; Zhao et al., 2020). Consequently, unpredictable macro-scale mechanical responses result (Huang et al., 2008; Gutierrez et al., 2009; Maeda et al., 2010; Gong and Liu, 2017; Bao et al., 2020; Nie ZH et al., 2020; Nie JY et al., 2021; Thakur and Penumadu, 2021; Wen et al., 2021; Wu et al., 2021; Yin et al., 2021). Particle morphology also plays a crucial role in particle kinematics and breakage and thus should be involved in the investigation of granular soils.

In recent years, the development of many optical and imaging techniques, such as stereomicroscope (Cho et al., 2006), QicPic apparatus (Altuhafi and Coop, 2011), stereophotography (Zheng and Hryciw, 2017), and X-ray micro-computed tomography (μCT) (Wu et al., 2012; Viggiani et al., 2015; Zhao and Wang, 2016), makes it possible to extract high-resolution particle morphology of granular soils and further investigate multiscale particle morphology. In this context, a significant body of research on the macro-micro mechanical responses of granular soils have emerged, including particle morphology description (Fonseca et al., 2012; Zhou et al., 2015; Zhao and Wang, 2016; Fei and Narsilio, 2020; Xiong et al., 2020; Nie et al., 2021; Thakur and Penumadu, 2021), particle kinematics (Hall et al., 2010; Hasan and Alshibli, 2010; Andrade et al., 2011; Cheng and Wang, 2018b), particle breakage (Alikarami et al., 2015; Zhao et al., 2015; Karatza et al., 2018), energy dissipation (Wang and Yan, 2012; Zhang et al., 2013), and fabric evolution (Maeda et al., 2010; Fonseca et al.,

✉ Jian-feng WANG, jefwang@cityu.edu.hk
Wei XIONG, https://orcid.org/0000-0003-0260-8776
Jian-feng WANG, https://orcid.org/0000-0002-6392-218X

Received Apr. 23, 2022; Revision accepted July 4, 2022;
Crosschecked Aug. 23, 2022; Online first Sept. 27, 2022

2013; Cheng and Wang, 2018a). Since particle morphology is multiscale in nature from the general form at a large length scale to the surface texture at a small length scale, this intrinsic characteristic encouraged us to explore and further compare the effects of particle morphology at different length scales on the macro-micro mechanical behaviours of granular soils. However, most studies have used an overall regularity descriptor, the average of several traditional descriptors at different length scales, to describe particle morphology (Yang and Luo, 2015; Xiao et al., 2019; Nie et al., 2021) or have focused on particle morphology at one specific length scale without considering other length scales (Gong and Liu, 2017; Nie et al., 2020). The possibly distinct contributions of particle morphology at different length scales have not been well explored and compared.

The discrete element method (DEM), first proposed by Cundall and Strack (1979), gives an alternative way to explore the role that particle morphology plays in the macro-micro mechanical responses of granular soils. To consider the effects of particle morphology, early DEM studies employed rheology-type rolling resistance models (Iwashita and Oda, 2000; Zhou et al., 2013) or incorporated simplified non-spherical particles (Rothenburg and Bathurst, 1991; Lin and Ng, 1997; Ng, 2009; Stroeven et al., 2011; Azéma et al., 2013; Nassauer et al., 2013; Kuhn et al., 2015; de Bono and McDowell, 2020; Jin et al., 2021), while more modern DEM models have considered sophisticated and realistic particle morphology (Kawamoto et al., 2018; Wu et al., 2021). In this context, many particle reconstruction techniques have been proposed to incorporate realistic particle morphology into DEM (Grigoriu et al., 2006; Liu et al., 2011; Mollon and Zhao, 2014; Zhou and Wang, 2017; Wei et al., 2018; Sun and Zheng, 2021; Xiong and Wang, 2021; Wang et al., 2022). Among them, the spherical harmonic (SH) is widely used. The SH coefficients obtained from realistic particle surface data contain all the morphological information at different length scales and hence can be treated as the "morphological gene" (Sun and Zheng, 2021). With the spherical harmonic-based principal component analysis (SH-PCA), the morphological genes and the corresponding morphological features at a particular length scale can be easily modified, leading to the "gene mutation" of a given particle (Xiong and Wang, 2021).

In this work, 27 DEM samples were generated with a reconstruction framework that incorporated the X-ray μCT, SH-PCA, and DEM to investigate the effects of particle morphology on the macro-micro mechanical responses of granular soils. Based on the authors' previous work on the one-to-one mapping and modelling of sand particles (Wu et al., 2021), it is a significant new step toward exploring and comparing the effects of particle morphology at different length scales using a novel particle reconstruction technique.

2 Data preparation framework

2.1 Morphology reconstruction by X-ray μCT and spherical harmonic analysis

Because of the 3D, high-resolution, and non-destructive merits (Xiong and Wang, 2021), X-ray μCT was adopted to extract the morphological data of sand particles in a small sample (i.e., diameter of 8 mm and height of 16 mm). The model contains around 1500 Leighton Buzzard Sand (LBS) particles with a diameter range of 600–1200 μm. The whole experiment was conducted using the synchrotron-based μCT scanner at the BL13W beamline of the Shanghai Synchrotron Radiation Facility (SSRF). The X-ray energy and voxel size were set to be 25 keV and 6.5 μm, respectively (Cheng and Wang, 2018a). After scanning, a series of image processing steps and analyses were needed to extract the target particle morphological data from the raw projection slices (Otsu, 1979; Perona and Malik, 1990; Chen et al., 2012). A more detailed description of the experimental device, testing procedure, and image processing work can be found in (Cheng et al., 2020a).

A 3D point cloud represented the obtained μCT-reconstructed particles. Each particle can then be expressed through spherical harmonic analysis (SHA) by a series of SH coefficients. Here, we briefly introduce the SHA procedure; a more detailed description can be found in (Zhou et al., 2015). The main functions of SHA are as follows:

$$\boldsymbol{r}(\theta, \varphi) = \sum_{n=0}^{\infty} \sum_{m=-n}^{n} \boldsymbol{C}_n^m Y_n^m(\theta, \varphi), \tag{1}$$

where $\boldsymbol{r}(\theta, \varphi)$ is the polar radius with the corresponding spherical coordinates $\theta \in [0, \pi]$ and $\varphi \in [0, 2\pi]$,

$\boldsymbol{C}_n^m$ is the SH coefficient, and $Y_n^m(\theta, \varphi)$ is the SH function given by

$$Y_n^m(\theta, \varphi) = \sqrt{\frac{(2n+1)(n-m)!}{4\pi(n+m)}}\, P_n^m(\cos\theta)\, \mathrm{e}^{\mathrm{i}m\varphi}, \quad (2)$$

where n and m are respectively the frequency and the order of the associated Legendre function $P_n^m(x)$:

$$P_n^m(x) = \frac{(-1)^m}{2^n n!}(1-x^2)^{\frac{m}{2}}\frac{\mathrm{d}^{n+m}}{\mathrm{d}x^{n+m}}(x^2-1)^n. \quad (3)$$

Based on $\boldsymbol{C}_n^m$, the given particle surface can be reconstructed using Eq. (1). When the maximum SH frequency is 15 or greater, SHA has been proven to precisely reconstruct the general form (GF), the local roundness (LR), and the surface texture (ST) of any given particle (Zhou et al., 2018; Cheng et al., 2020b; Xiong et al., 2020).

2.2 Morphological gene mutation by SH-PCA

The SH-PCA is utilized in this study to implement morphological gene mutation. The main procedure of SH-PCA is briefly introduced below. The whole sample $\boldsymbol{B}$ can be expressed as:

$$\boldsymbol{B} = \left[\mathrm{real}\left(\boldsymbol{C}_{nj}^m\right), \mathrm{imag}\left(\boldsymbol{C}_{nj}^m\right)\right]^{\mathrm{T}}, \quad (4)$$

where each quantity in $\boldsymbol{C}_{nj}^m$ is a complex number with the format of $\alpha+\beta$i (i is the imaginary unit), j denotes particle j; real(*) and imag(*) extract the real and imaginary parts of each quantity, respectively. Any particle within the given sample can be expressed as:

$$\left(\boldsymbol{C}_{nj}^m\right)^{\mathrm{T}} = \boldsymbol{u}_{\boldsymbol{B}} + \boldsymbol{\sigma}_{\boldsymbol{B}}^2 \boldsymbol{y}, \quad (5)$$

where $\boldsymbol{u}_{\boldsymbol{B}}$ and $\boldsymbol{\sigma}_{\boldsymbol{B}}^2$ are the mean and the variance of $\boldsymbol{B}$, respectively, and $\boldsymbol{y}$ is a $2(n+1)^2\times1$ vector of the variation coefficients.

SH-PCA is then performed on $\boldsymbol{\sigma}_{\boldsymbol{B}}^2$. First, all the covariances of SH coefficients at different frequencies are set to zero. That is because Y_n^m with different frequencies are orthogonal, and hence the SH coefficients at two different frequencies should be irrelevant. By averaging with its transposed matrix, the obtained $\boldsymbol{\sigma}_{\boldsymbol{B}}^2$ is symmetrized. Then, the PCA is performed on $\boldsymbol{\sigma}_{\boldsymbol{B}}^2$ and the eigenvectors obtained are sorted in the decreasing order of the corresponding eigenvalue λ to form a principal component (PC) matrix $\boldsymbol{V}_{\mathrm{PC}}$. Based on the PC matrix obtained, any particles within the given sample can be reconstructed by

$$\boldsymbol{C}_{\mathrm{j}}^{\mathrm{T}} = \boldsymbol{u}_{\boldsymbol{B}} + \sqrt{\boldsymbol{\lambda}}\,\boldsymbol{V}_{\mathrm{PC}}\boldsymbol{y} = \boldsymbol{u}_{\boldsymbol{B}} + \sum_{t=1}^{R_{\mathrm{d}}} y_t\sqrt{\lambda_t}\,\boldsymbol{v}_{\mathrm{PC}t}, \quad (6)$$

where λ_t and $\boldsymbol{v}_{\mathrm{PC}t}$ are the tth eigenvalue and eigenvector, respectively; y_t is the tth variation coefficient in $\boldsymbol{y}$; R_{d} denotes the division of PC ranges for different length scales. $\boldsymbol{V}_{\mathrm{PC}}$ shows an additive feature of particle reconstruction: different PC ranges correspond to different length scales, and thus, the overall reconstruction is a step-by-step procedure from the large length scale to the small length scale (Xiong and Wang, 2021). Based on this characteristic, the morphological gene mutation that adds variance to particle morphology at different length scales can be readily implemented by

$$\boldsymbol{b}_{nj} = \boldsymbol{u}_{\boldsymbol{B}} + \chi_{\mathrm{a}}\sum_{t=1}^{20}\boldsymbol{b}_t + \chi_{\mathrm{b}}\sum_{t=21}^{30}\boldsymbol{b}_t + \chi_{\mathrm{c}}\sum_{t=31}^{73}\boldsymbol{b}_t + \chi_{\mathrm{d}}\sum_{t=74}^{91}\boldsymbol{b}_t + \cdots, \quad (7)$$

where $\boldsymbol{b}_t = y_t\sqrt{\lambda_t}\,\boldsymbol{V}_{\mathrm{PC}t}$ reflects the initially reconstructed particle, χ is the scaling factor, and its subscript denotes the target scale range. Furthermore, the relationship between PC range and morphological length scale is obtained through a parametric analysis of all these scaling factors. Specifically, each scaling factor is set to be 0.5 and 1.5, respectively, to form in total eight groups of granular assemblages. Then four traditional morphology descriptors are utilized to describe the morphological variance of all these granular assemblages at different length scales, i.e., the aspect ratio AR reflects the GF of particle morphology, the roundness R for LR and the overall shape parameters like sphericity and convexity for all length scales (the definitions of all morphology descriptors are given in electronic supplementary materials). Fig. 1 shows the cumulative frequencies of different morphology descriptors with downscaled or upscaled scaling factors. It is found that 1–20 PCs contribute the most to the formation of GF, while 31–73 PCs contribute the most to LR. Thus, χ_{a} and χ_{c} are responsible for GF and LR, respectively. A more detailed description of SH-PCA can be found in (Xiong and Wang, 2021).

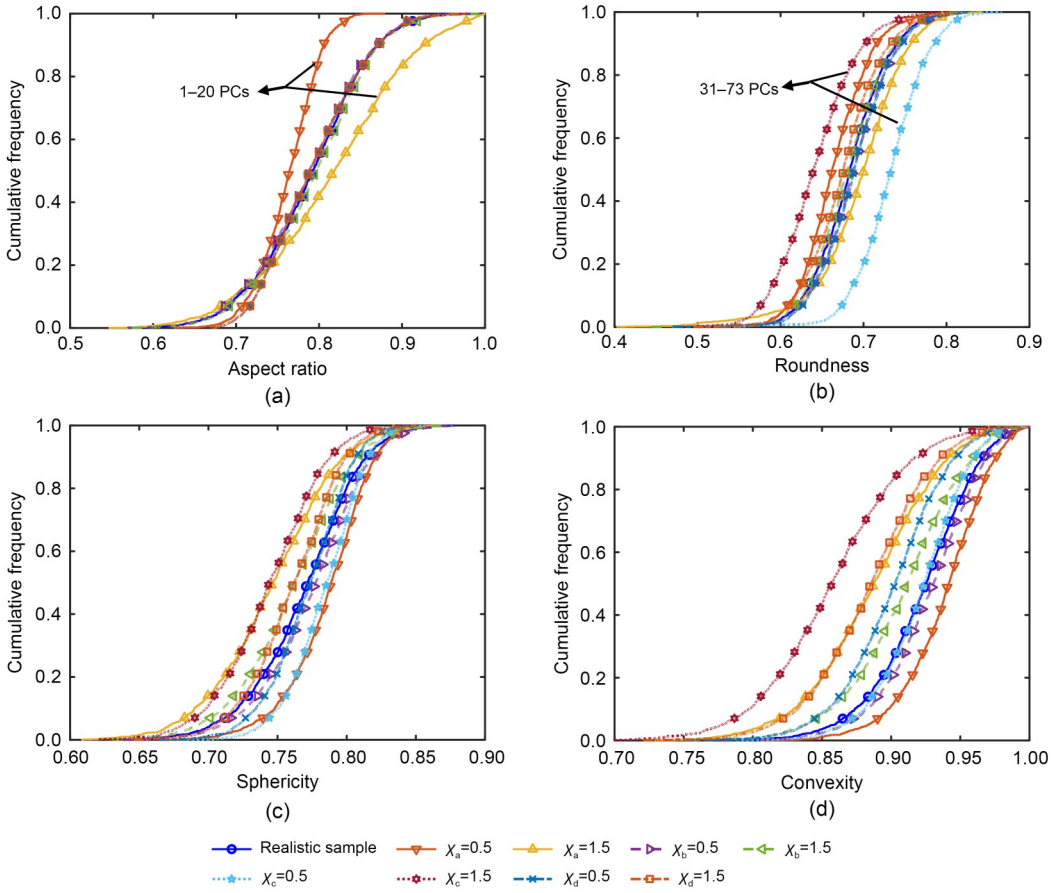

Fig. 1 Cumulative frequency of morphology descriptors with varying different scaling factors: (a) aspect ratio AR; (b) roundness *R*; (c) sphericity *S*; (d) convexity C_x

2.3 DEM modelling technique

To illustrate the effect of the morphological gene mutation at a specific length scale, one particle was chosen from the experimental database as an example. Fig. 2 shows the morphological gene-mutated particles generated with varying scaling factors χ_a and χ_c. Specifically, χ_a and χ_c in Eq. (7) are set to 0.00, 0.25, 0.50, 0.75, 1.25, and 1.50, respectively, to achieve different degrees of morphological gene mutation. The reference particle corresponds to χ_a=χ_c=1.0 in Fig. 2. Table 1 shows the traditional morphology descriptors for all the morphological gene-mutated particles. From Table 1, the morphological gene mutation at GF-level (GF-GM) witnesses an increase in elongation, flatness, and aspect ratio with χ_a increasing from 0.0 to 1.5, which corresponds to the phenomenon shown in Fig. 2, i.e., the particle GF-GM with χ_a=1.5 is rougher and more irregular than GF-GM with χ_a=0.0. With GF-GM, *R* shows a fluctuation around 0.6. It is because the GF-level morphology will affect the largest inscribed sphere radius in calculating *R*. In addition, the morphological gene mutation at LR-level (LR-GM) witnesses a decreasing roundness with χ_c varying from 0.0 to 1.5, while showing no effects on morphology descriptors at GF-level. Obviously, the particle surface of LR-GM with χ_c=1.50 is rougher with sharper corners than LR-GM with χ_c=0.0.

All the resulting gene-mutated particles were imported into PFC^{3D} to build DEM particles with the bubble-packing algorithm. The two parameters, namely, the radius ratio of the smallest to the largest sphere ρ and the sphere-to-sphere intersection angle ϕ, are set to be ρ=0.3 and ϕ=150° (Wu et al., 2021). Fig. 3 compares two DEM samples, namely, LR-GM with χ_c=0.0 and LR-GM with χ_c=1.5, to visualize the distinction between different samples. Obviously, LR-GM with χ_c=1.5 shows a much rougher surface but similar GF when compared with LR-GM with χ_c=0. Note that the realistic volume list extracted from

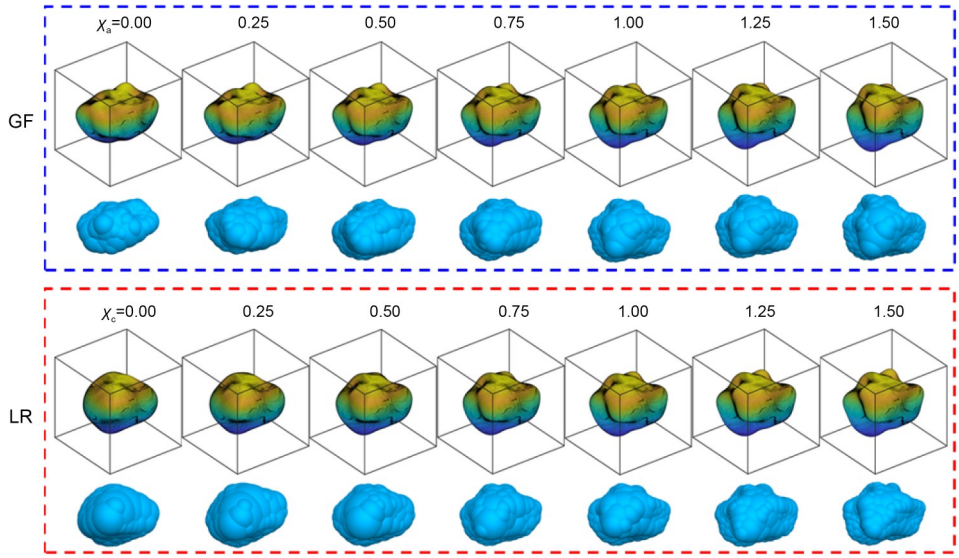

Fig. 2 Reconstruction of morphological gene-mutated samples and the corresponding representations in the discrete element method

Table 1 Morphology descriptors for gene-mutated particles

Item	χ_a, χ_c	Elongation	Flatness	Aspect ratio	Roundness	Sphericity	Convexity
GF-GM	0.00	0.755	0.766	0.761	0.676	0.822	0.933
	0.25	0.775	0.821	0.798	0.648	0.826	0.933
	0.50	0.803	0.871	0.837	0.619	0.827	0.926
	0.75	0.845	0.906	0.875	0.594	0.823	0.914
	1.00	0.890	0.935	0.912	0.582	0.815	0.899
	1.25	0.936	0.959	0.947	0.598	0.804	0.879
	1.50	0.982	0.978	0.980	0.620	0.789	0.858
LR-GM	0.00	0.890	0.935	0.912	0.731	0.854	0.952
	0.25	0.890	0.935	0.912	0.710	0.852	0.949
	0.50	0.890	0.935	0.912	0.672	0.844	0.937
	0.75	0.890	0.935	0.912	0.620	0.831	0.920
	1.00	0.890	0.935	0.912	0.582	0.815	0.899
	1.25	0.890	0.935	0.912	0.566	0.796	0.874
	1.50	0.890	0.935	0.912	0.554	0.775	0.848

the μCT experiment was utilized in all samples, as shown in Fig. 3b.

To prepare the samples with predefined confining stresses for the triaxial shear, two different servo-control mechanisms were needed. First, all the samples were loaded to the predefined axial and confining stresses (equal to 1.5 MPa in this study) by adopting the conventional servo-wall mechanism (Fig. 3d). The friction coefficient μ of all particles was set to control the packing density for a given sample. After that, the rigid cylinder wall was deleted, and the bonded-ball membrane was installed (Fig. 3e). The radius of the membrane boundary should be slightly larger than that of the rigid cylinder wall boundary due to the thickness of the membrane, and this gap was empirically set to be 0.90–0.95 times the ball radius (Qu et al., 2019). External equivalent forces were then assigned to all the membrane balls between the two loading platens to simulate the hydrostatic loading on the membrane during the physical triaxial test. The external equivalent force F_e on each membrane ball is calculated according to Eq. (8) (Fazekas et al., 2006; de Bono et al., 2012; de Bono and McDowell, 2014; Qu et al., 2019):

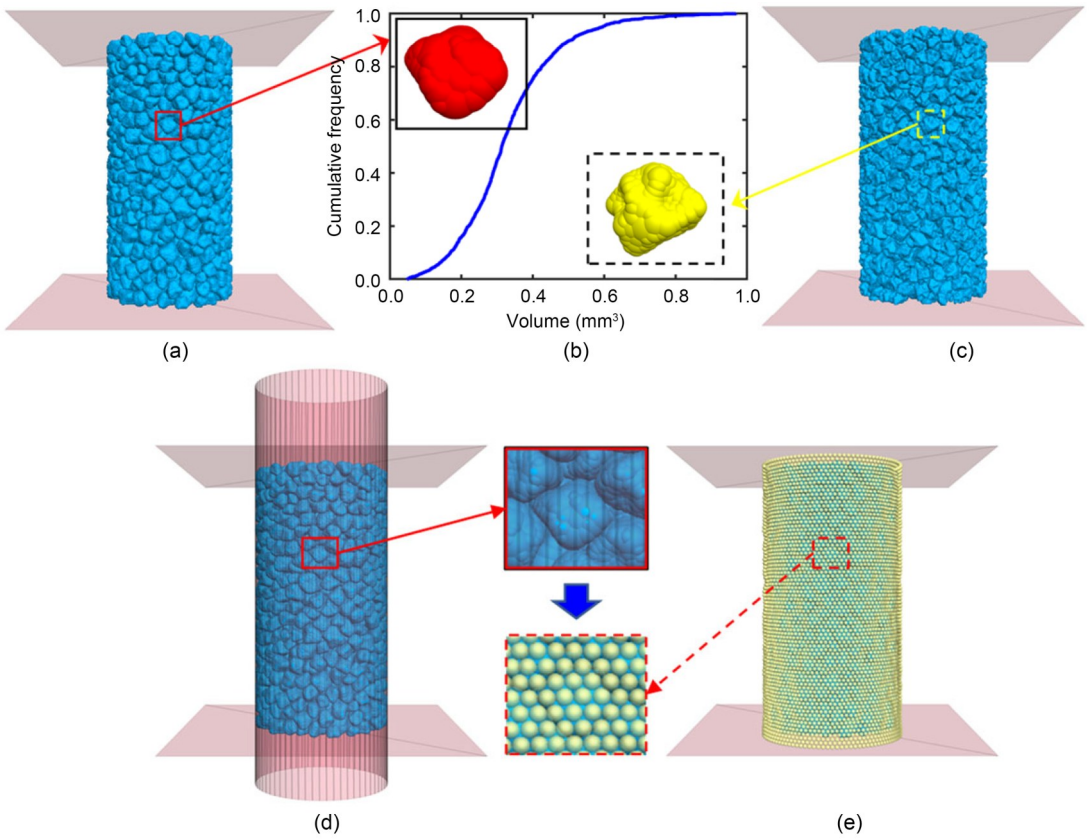

Fig. 3 DEM modelling technique with morphological gene mutation: (a) LR-GM with χ_c=0.0; (b) real volume distribution; (c) LR-GM with χ_c=1.5; (d) rigid servo-wall; (e) membrane servo-wall

$$F_e = \frac{\sigma_c}{3}\sum_i^6 \boldsymbol{n}_i S_{Ai}, \tag{8}$$

where σ_c is the confining stress, and S_{Ai} and $\boldsymbol{n}_i$ are the surface area and the unit normal vector of the ith neighboring triangle, respectively. Since the bonded-ball membrane will deform with loading, F_e on each ball was calculated and updated after every 100 timesteps. All the samples were ready for the triaxial shear after being reiterated to achieve a state of equilibrium.

2.4 Sample description and model parameters

A total of 27 samples were generated and divided into three groups: a one-to-one mapping sample, 13 random relatively denser packing samples (RDPS), and 13 random relatively looser packing samples (RLPS). In the one-to-one mapping sample, particles share the same volumes and spatial locations as the physical ones from the X-ray μCT experiment. RDPS and RLPS were generated by setting μ=0.0 and 0.5 during the sample compaction process. Thus, these two groups share the same particle set but different initial void ratios. Since it is very difficult to generate a loose sample with realistic particles under a confining pressure of 1.5 MPa, all samples of RDPS and RLPS are medium dense samples with relatively denser and looser packing states. To simplify the DEM simulation and highlight the effects of particle morphology at different length scales, each sample of both RDPS and RLPS contains one type of morphological gene-mutated particle with χ_a and χ_c varying from 0.0 to 1.5 for GF and LR, respectively. Note that all samples in both groups obey the same volume distribution as in the X-ray μCT experiment.

Table 2 lists the model parameters after calibration, and follows Wu et al. (2021) and de Bono and McDowell (2014). This sample was compacted with predefined confining stresses by adopting the above-mentioned bonded-ball membrane technique. The top and bottom platens were then loaded simultaneously toward each other with a constant velocity of 0.005 m/s to an ultimate axial strain of 30% for both RDPS and

Table 2 DEM model parameters

Item	Description
Sample parameter	
Size: height×diameter (mm)	16×8
Number of clumps	1520
Density (kg/m^3)	2650
Local damping coefficient	0.7
Clump friction	0.3
Wall friction	0.0
Contact model	Hertz-Mindlin
Shear modulus (GPa)	28
Poisson's ratio	0.25
Membrane parameter	
Number of balls	7600
Density (kg/m^3)	1000
Tensile strength (N)	1×10^{200}
Tangential strength (N)	1×10^{200}
Normal stiffness (N/m)	1×10^{6}
Shear stiffness (N/m)	1×10^{6}
Ball radius (mm)	0.128

RLPS. According to Wu et al. (2021), the chosen parameters and contact types can lead to a model response that matches well with the experimental results. Fig. 4 shows the comparison of the stress-strain curve and the 3D rose map of the one-to-one mapping sample with those from the X-ray μCT experiment (Wu et al., 2021). The excellent agreement between numerical and experimental results validates the model parameters chosen in this study.

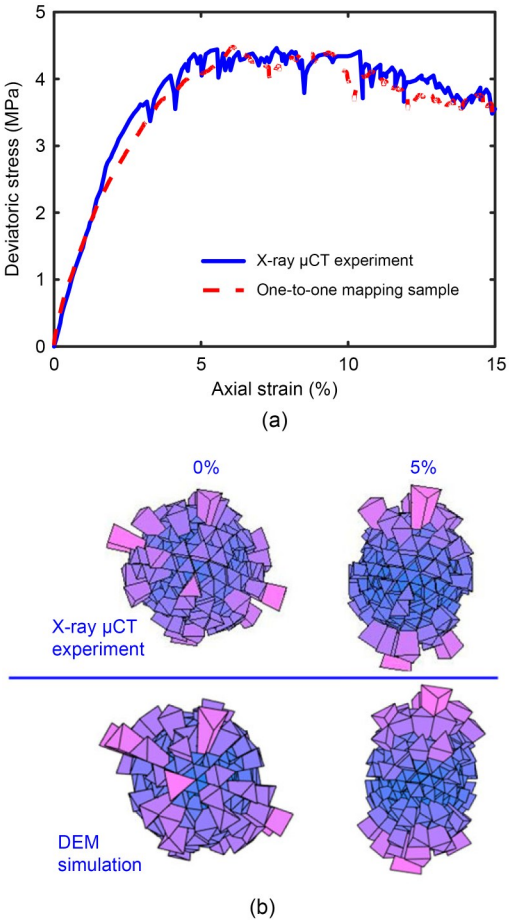

Fig. 4 Model validation: (a) stress-strain curve; (b) 3D rose map

3 Numerical results and discussion

3.1 Stress-strain relationship

Fig. 5 illustrates the relationships between stress ratio (deviatoric stress (q)/mean stress (p)) and axial strain ε_L for both RDPS and RLPS. Here, q, p, and ε_L are defined as follows:

$$q=\frac{\sigma_1-\sigma_3}{2}, \tag{9}$$

$$p=\frac{\sigma_1+2\sigma_3}{3}, \tag{10}$$

$$\varepsilon_L=\frac{h_0-h}{h_0}, \tag{11}$$

where σ_1 is the axial stress, σ_3 is the confining stress, h_0 is the initial sample height, and h is the sample height at the deformed state. From Fig. 5a, all curves in RDPS share a similar overall variation trend regardless of the variance of particle morphology involved. They show a continuous strain hardening response to the peak state at an axial strain of around 5% and a mild strain-softening up to the advent of the critical condition. It is found that the initial stiffness, peak state stress ratio, and critical state stress ratio among different morphological gene-mutated samples are consistent and vary in a narrow range. This indicates that the particle morphology shows a negligible effect on the stress-strain responses of granular soils in a relatively denser packing state. This finding agrees well with the experimental results of Sharma et al. (2021) and the numerical results of Qu et al. (2022).

Compared to RDPS, all RLPS in Fig. 5b exhibit a lesser initial stiffness, a more delayed peak state (at an axial strain of around 8%), and a milder strain-softening up to the critical state. A notable difference

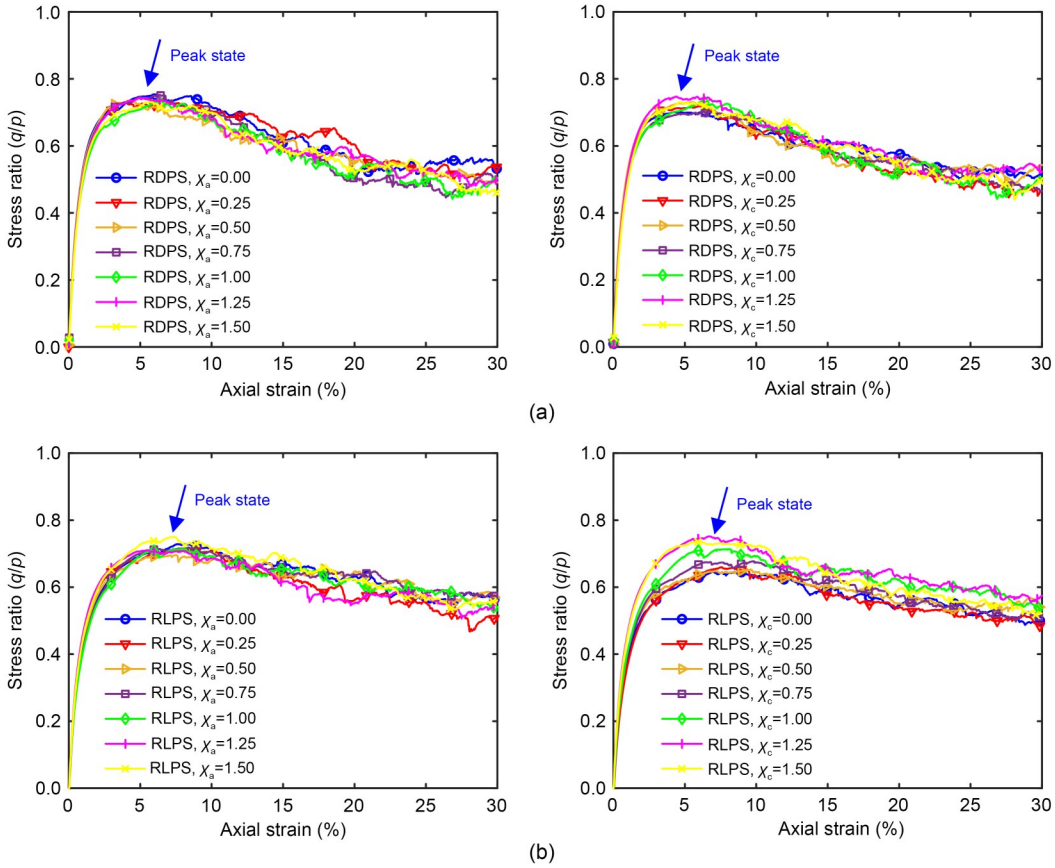

Fig. 5 Stress-strain responses of both RDPS and RLPS: (a) morphological gene mutation of RDPS; (b) morphological gene mutation of RLPS

in the initial stiffness and peak state stress ratio can be found among samples with morphological gene mutation at LR-level and a smaller difference at GF-level. This exciting finding implies that the particle morphology at LR-level plays a more significant role in the stress-strain response at the pre-peak stage than the particle morphology at GF-level. Furthermore, the larger the scaling factor is, the more prominent the peak state stress ratio is. That is because a more prominent scaling factor leads to less roundness with more sharp corners and edges at LR-level. The overall rougher particle surface obtained results in less particle translation and rotation at the grain-scale and, consequently, a more prominent peak state stress ratio. It is worth noting that the sample with χ_c=1.25, instead of the one with χ_c=1.50, shows the highest peak state stress ratio for both RDPS and RLPS. That is probably because the relatively larger initial void ratio of the sample with χ_c=1.50 outperforms the rough particle surface, resulting in a lower peak state stress ratio.

3.2 Volumetric strain

Fig. 6 shows the volumetric strain against the axial strain relationships of both RLPS and RDPS groups. The volumetric strain ε_v is defined as follows:

$$\varepsilon_v = \frac{\Delta V}{V_0} = \frac{\pi(R_0+\Delta R)^2(h_0+\Delta h)-\pi R_0^2 h_0}{\pi R_0^2 h_0} = 2\varepsilon_R+\varepsilon_L+\varepsilon_R^2+2\varepsilon_R\varepsilon_L+\varepsilon_R^2\varepsilon_L, \quad (12)$$

where ΔV, ΔR, and Δh are the increments of the sample volume, average membrane radius, and sample height at the deformed state, while V_0, R_0, and h_0 denote the corresponding values at the initial state; ε_R and ε_L are the radial and the axial strains expressed by $\varepsilon_R=\Delta R/R_0$ and $\varepsilon_L=\Delta h/h_0$, respectively. Note that the higher-order terms in Eq. (12) cannot be neglected in a large-strain problem such as the one studied here. RDPS show a consistent evolution trend of volumetric strain against axial strain, regardless of the morphological gene mutation at GF- or LR-level (Fig. 6a). In

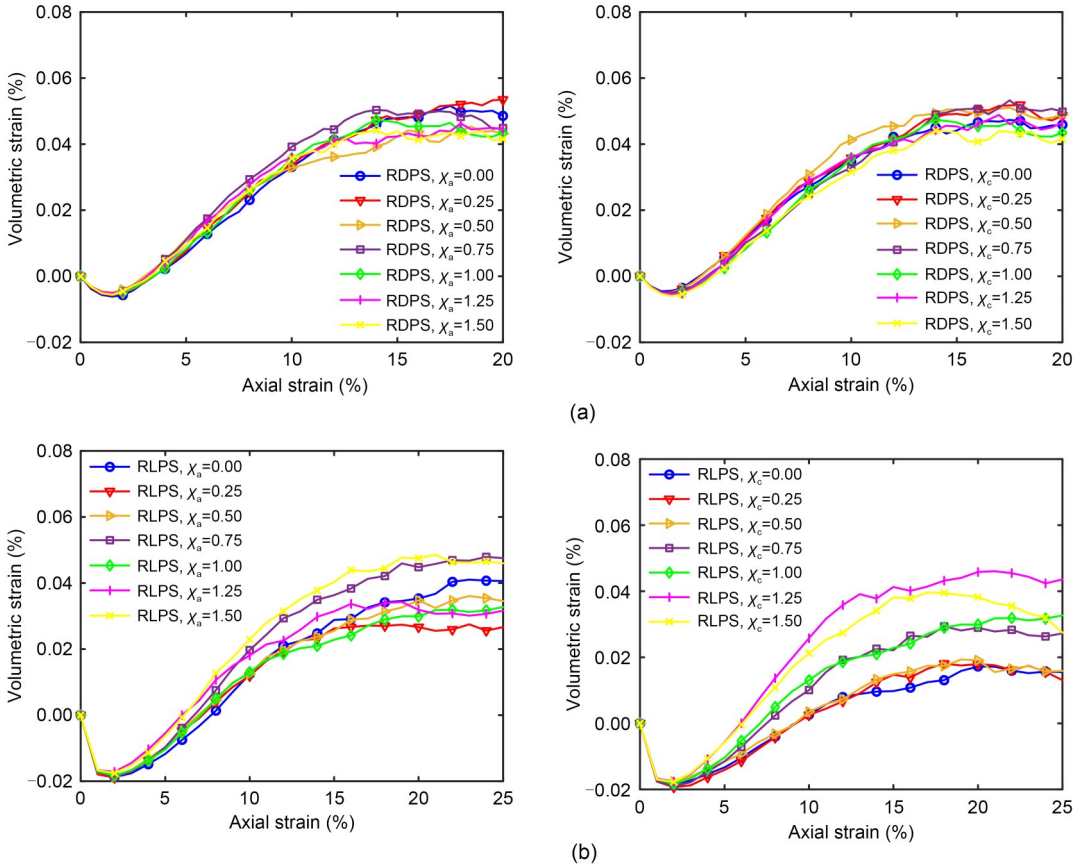

Fig. 6 Volumetric strain evolution of both RDPS and RLPS: (a) morphological gene mutation of RDPS; (b) morphological gene mutation of RLPS

general, RDPS exhibit a slight initial contraction and then a substantial dilation which gradually diminishes towards the critical state while the volumetric strain remains nearly constant. It is found that particle morphology only shows a slight effect on the evolution of volumetric strain against axial strain for RDPS. This is because all the samples in RDPS are compacted to their densest packing state by setting the interparticle friction coefficient to zero. The dense packing-induced high interlocking of particles constrains the rotation and translation of particles within the given sample. Hence, particle morphology plays a minor role in the evolution of volumetric strain against axial strain.

Compared to RDPS, all RLPS witness a more significant initial contraction and a notable difference in volumetric strain curves among different morphological gene-mutated samples (Fig. 6b). This observation implies that particle morphology plays a more prominent role in the volumetric strain behaviour in RLPS than in RDPS. This is because the relatively looser packing state of RLPS provides more space for particles to rotate and translate, making particle morphology more influential on the volumetric behaviour of RLPS. In addition, RLPS with morphological gene mutation at GF-level show a relatively consistent variation trend of volumetric strain at the early stage of axial strain (before 10%), and the difference of curves among different gene-mutated samples becomes more significant at large strains. It is interesting to note that RLPS with morphological gene mutation at LR-level show a notable difference in the volumetric strain curves at the early stage of axial strain and the difference remains roughly constant to the final critical state. This observation implies that the LR-level particle morphology contributes more to the early stage of volumetric strain evolution, while the GF-level particle morphology plays a more significant role in the later stage. Specifically, at the early stage of axial strain, the particles are inclined to rotate with the expansion of sample volume, in which the LR-induced particle interlocking plays a more significant role. With the continuous expansion of sample volume at the later

stage, particles have more space to rotate and translate; hence, the GF-induced particle interlocking contributes more.

3.3 Initial void ratio

RDPS and RLPS were generated by setting the friction coefficient μ of all particles to be μ=0.0 and 0.5, respectively, during the compaction process. Table 3 shows the initial void ratios for different morphological gene-mutated samples. Here, χ_a and χ_c are the scaling factors governing the morphological gene mutation at GF and LR, respectively. It is found that RLPS show a generally larger initial void ratio than RDPS and the larger the scaling factor is, the more prominent the initial void ratio is. The reason is that, for RDPS, the more prominent scaling factor leads to a more irregular particle surface at the targeting length scale, making it harder to compact. Similarly, RLPS with rougher particle surfaces contain more interparticle contacts, and so more frictional work is needed during the compaction process with the same interparticle friction coefficient. The relationship between initial void ratios and traditional morphology descriptors for different morphological gene-mutated samples is shown in Fig. 7. More precisely, the initial void ratio increases with the increasing aspect ratio and

Table 3 Initial void ratio of virtual samples

Group		Initial void ratio						
		χ_a, χ_c=0.00	χ_a, χ_c=0.25	χ_a, χ_c=0.50	χ_a, χ_c=0.75	χ_a, χ_c=1.00	χ_a, χ_c=1.25	χ_a, χ_c=1.50
RDPS	GF	0.358	0.355	0.358	0.360	0.365	0.365	0.376
	LR	0.330	0.339	0.346	0.350	0.365	0.377	0.388
RLPS	GF	0.390	0.391	0.392	0.393	0.395	0.393	0.396
	LR	0.386	0.389	0.389	0.390	0.395	0.398	0.407

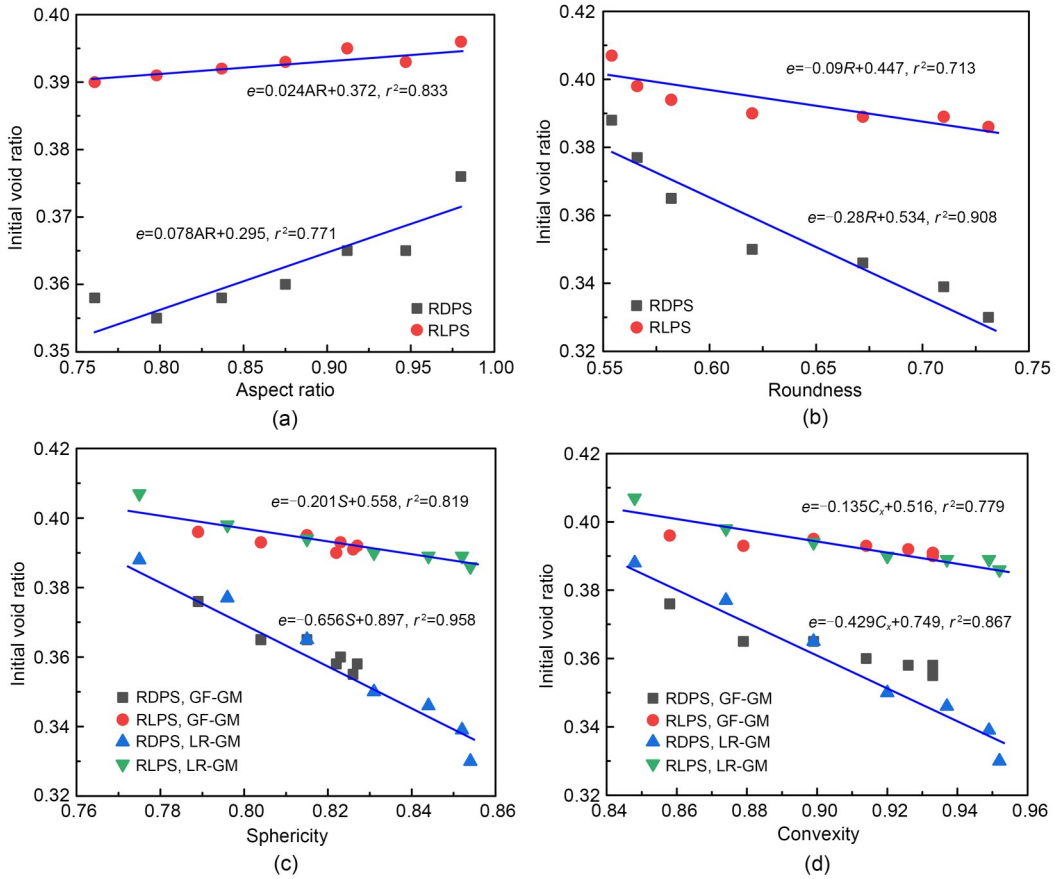

Fig. 7 Relationship of initial void ratio *e* and traditional morphology descriptors: (a) aspect ratio AR; (b) roundness *R*; (c) sphericity *S*; (d) convexity C_x

shows an opposite decreasing trend with the increase of roundness (Figs. 7a and 7b). Also, RDPS experience a larger rate of variation of initial void ratio than RLPS for both aspect ratio and roundness. For the overall shape parameters like sphericity and convexity (Figs. 7c and 7d), the initial void ratio decreases with both the increasing sphericity and convexity. Similar to the aspect ratio and roundness, RDPS show a faster variation of initial void ratio with the overall shape parameters than RLPS do, regardless of the morphological gene mutation at different length scales.

3.4 Energy dissipation behaviour

Particles within a given sample can rotate and translate throughout the whole triaxial shearing process and such grain-scale behaviours may consequently affect the macro-scale responses of granular soils. Since any individual particle needs to consume energy to move, the energy dissipation of the whole granular system is important for us in understanding the macro- and micro-scale mechanical behaviours of granular assemblages. Based on the law of energy conservation, the following equation (Wang and Yan, 2012) should be satisfied at any stage of triaxial shearing:

$$\mathrm{d}W+\mathrm{d}W_{\mathrm{g}}=\mathrm{d}E_{\mathrm{s}}+\mathrm{d}E_{\mathrm{k}}+\mathrm{d}E_{\mathrm{f}}+\mathrm{d}E_{\mathrm{d}}, \tag{13}$$

where W is the boundary work (which is equal to the sum of work done by the axial loading W_{w} and confining pressure W_{m}); W_{g} is the body work done by gravity; E_{s} is the elastic strain energy; E_{k} is the kinetic energy; E_{f} is the frictional energy dissipation; E_{d} is the damping dissipation. Note that the energy dissipation due to particle breakage is not included in Eq. (13) because particle breakage is not considered in the DEM simulations of this study. This is justified by the negligible amount of particle breakage observed in the X-ray μCT study on the LBS sample done by Cheng and Wang (2018b). Herein, the PFC^{3D} built-in fish functions, i.e., clump.energy, ball.energy, contact.energy.sum, were utilized to extract the energy storage/dissipation components at each state of triaxial shearing.

Fig. 8 compares the various incremental energy components of both RDPS and RLPS with $\chi_{\mathrm{a}}=\chi_{\mathrm{c}}=1.0$. Note that the incremental axial strain was set to be 1%. In general, energy conservation can be found in both RDPS and RLPS during triaxial shear. Specifically,

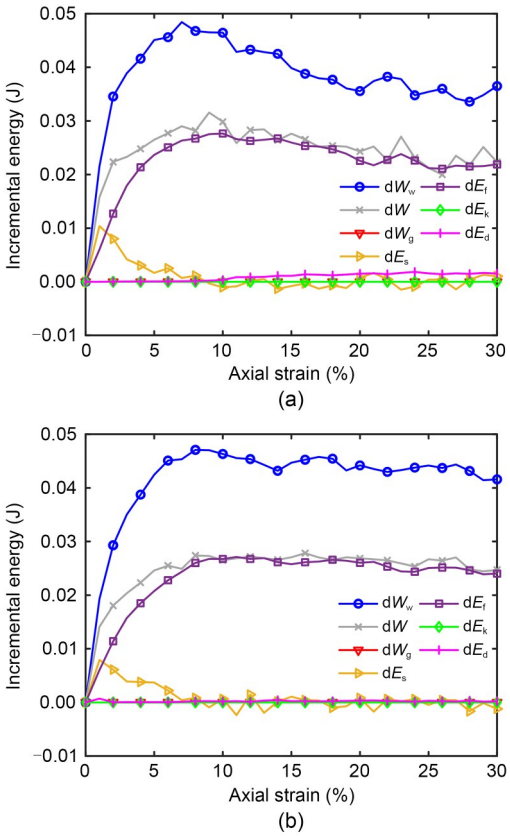

Fig. 8 Incremental energy components for RDPS and RLPS with $\chi_{\mathrm{a}}=\chi_{\mathrm{c}}=1.0$: (a) RDPS; (b) RLPS

the incremental elastic energy $\mathrm{d}E_{\mathrm{s}}$, except for the first few percentages of axial strain, fluctuates around zero regardless of the initial void ratio involved. This phenomenon implies that the granular assemblage has little capability to store elastic strain energy at larger axial strains. Compared to RDPS, RLPS show a slightly smaller peak incremental elastic strain energy $\mathrm{d}E_{\mathrm{s}}$ at smaller axial strains and a milder change of both incremental boundary work $\mathrm{d}W$ and incremental frictional energy dissipation $\mathrm{d}E_{\mathrm{f}}$ after the peak state. Due to the quasi-static nature of the simulations, the incremental kinetic energy $\mathrm{d}E_{\mathrm{k}}$ remains around zero. The incremental body work $\mathrm{d}W_{\mathrm{g}}$ is also zero for both RDPS and RLPS because the gravity acceleration is set to zero. Therefore, the incremental boundary work $\mathrm{d}W$ is mainly transformed into the grain-scale elastic strain at the early stage of shearing and later mainly dissipated by interparticle friction at larger axial strains. The incremental damping energy $\mathrm{d}E_{\mathrm{d}}$ is negligibly small when compared with other energy components. This is because the average unbalanced forces of all samples are less than 5×10^{-4} N at any stage of triaxial

shearing due to the quasi-static nature of the simulation, and thus the generalized damping forces, which are applied to all six degrees of freedom of any particle and are proportional to the total unbalanced force, are very small.

Fig. 9 compares the incremental frictional energy dissipation dE_f for both RDPS and RLPS with various levels of morphological gene mutation. It is found that the dE_f curve from each simulation is basically consistent with its corresponding stress ratio curve shown in Fig. 5, reflecting the major role of interparticle friction in dissipating the input boundary work throughout most of the shearing process. Evidently, as shown in Fig. 9a, the morphological gene mutation, either at the general form or at the local roundness level, shows little influence on the initial slope of the dE_f curve (i.e., <3% strain) of both RDPS and RLPS. This is because the boundary work is mainly stored as interparticle elastic energy during this stage. The morphological gene mutation starts to affect the dE_f curve after about 3% strain, and the level of influence is apparently more pronounced in RLPS than in RDPS, particularly at the large-strain stage (i.e., >10% strain) (Fig. 9b). This is perhaps due to the larger degrees of freedom of the particles in the RLPS. Another notable observation for RLPS is that the gene mutation at the LR-level shows a higher level of influence on the dE_f curve (with the peak of dE_f occurring earlier and being larger) than that at the GF-level. A larger scaling factor of gene mutation generally results in a larger influence on the peak dE_f behaviour (Fig. 9b) than those at the GF-level.

Additionally, the variations of particle morphology and initial void ratio can strengthen or relieve the degrees of freedom of particles in a given granular assemblage and consequently affect the energy storage/dissipation behaviour. Thus, the final incremental frictional dissipation obtained should be a competition of the two controlling variables. Since particle morphology at the LR-level outperforms that at the GF-level in affecting the peak incremental frictional energy dissipation, only roundness is utilized in the following

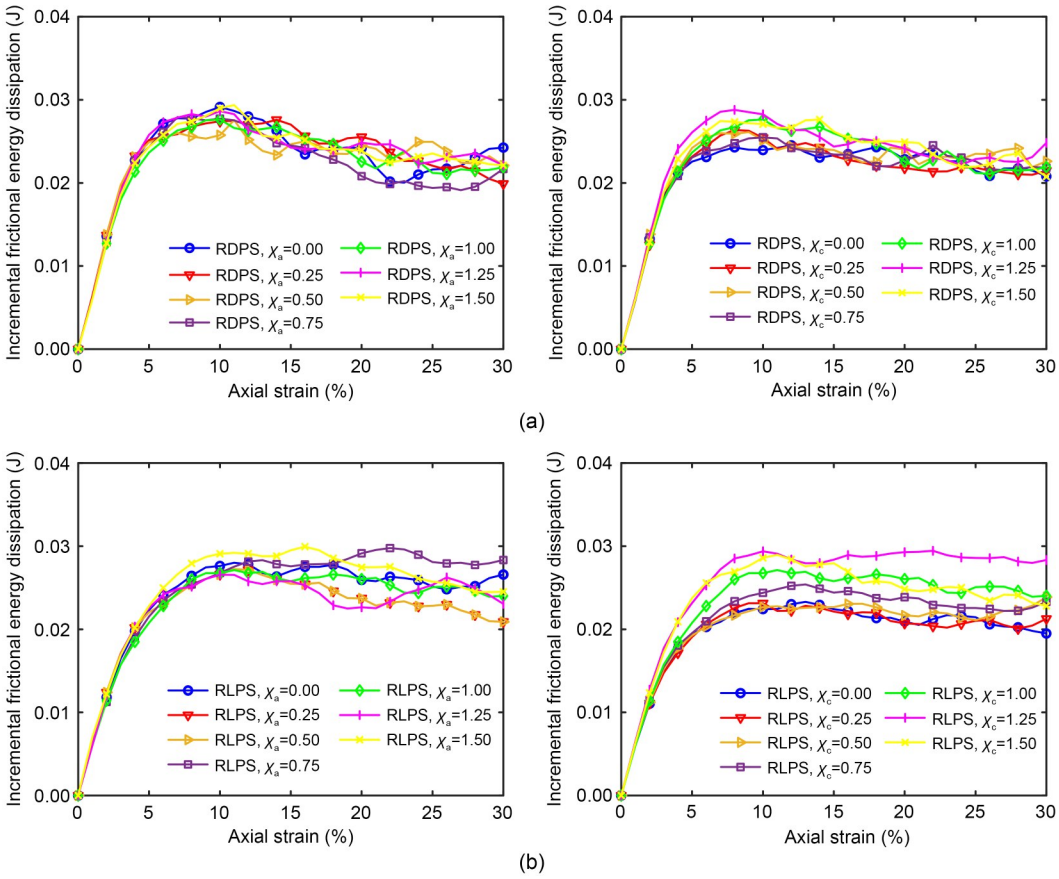

Fig. 9 Energy dissipated by interparticle friction: (a) morphological gene mutation of RDPS; (b) morphological gene mutation of RLPS

analysis. Eq. (14) is proposed to correlate the peak incremental frictional energy dissipation, roundness, and initial void ratio:

$$\mathrm{d}E_{\mathrm{fp}} = a + bR + cR^2 + \frac{d}{e} + \frac{f}{e^2} + \frac{g}{e^3}, \qquad (14)$$

where $\mathrm{d}E_{\mathrm{fp}}$ is the peak incremental frictional energy dissipation; a, b, c, d, f, and g are the fitting coefficients whose values are 2.78, −0.34, 0.24, −2.92, 1.08, and −0.13, respectively. The r^2 of the surface fitting is 0.886, reflecting a good agreement between the fitting surface and the original data points. Fig. 10 shows the fitting surface, original data points, and the fitting errors (expressed by small vertical lines). In general, $\mathrm{d}E_{\mathrm{fp}}$ increases with decreasing R. It is because the smaller R will result in more sharp corners and edges of particles, and consequently more interparticle contacts. Compared to R, e shows a more complex trend of variation against $\mathrm{d}E_{\mathrm{fp}}$. $\mathrm{d}E_{\mathrm{fp}}$ shows an increasing trend with increasing e at small initial void ratios but an opposite trend at large initial void ratios. The explanation of this phenomenon is that, at small initial void ratios, an increase of e relieves the degrees of freedom of particles and hence increases $\mathrm{d}E_{\mathrm{fp}}$ while, at large initial void ratios, a further increase of e leads to the loss of interparticle contacts and hence decreases $\mathrm{d}E_{\mathrm{fp}}$.

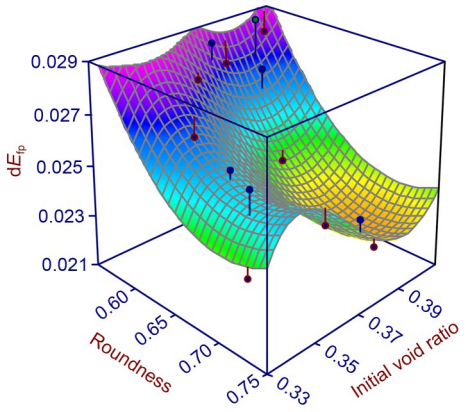

Fig. 10 Correlation of roundness, initial void ratio, and peak incremental frictional energy dissipation

4 Conclusions

In this study, the X-ray μCT, SH-PCA, and DEM were incorporated to generate morphological gene-mutated virtual samples at different length scales. The 27 DEM samples obtained were categorized into three groups, and the effects of particle morphology at different length scales on the stress-strain and energy storage/dissipation behaviours were carefully investigated. The main contributions and findings of this study are summarized as follow:

(1) Comparison of the simulation results from RDPS and RLPS indicates that the effects of particle morphology on the stress-strain, volumetric strain, and energy storage/dissipation responses are more pronounced for looser samples than for denser ones. Among different length scales, the particle morphological features at the LR-level outperform those at the GF-level in dictating the initial stiffness, peak state stress ratio, volumetric strain, and frictional energy dissipation behaviours.

(2) The frictional energy dissipation curves are consistent with the corresponding stress ratio curves for both RDPS and RLPS, reflecting the significant role of interparticle friction in dissipating the input boundary work throughout most of the shearing process. In addition, the peak incremental frictional energy dissipation is a result of the competition between particle morphology and the initial void ratio. It is found that the incremental frictional energy dissipation increases with decreasing roundness while showing an increasing trend with increasing initial void ratio at small initial void ratios but an opposite trend at larger initial void ratios.

Acknowledgments

This work is supported by the General Research Fund (Nos. CityU 11201020 and CityU 11207321) from the Research Grant Council of the Hong Kong Special Administrative Region (SAR), China, and the Contract Research Project (No. 9211295) from the Geotechnical Engineering Office of the Civil Engineering Development Department of the Government of the Hong Kong SAR, as well as the BL13W Beamline of Shanghai Synchrotron Radiation Facility (SSRF), China. The first author acknowledges the financial support from the Hong Kong PhD Fellowship Scheme (HKPFS).

Author contributions

Wei XIONG and Jian-feng WANG designed the research. Wei XIONG and Qi-min ZHANG processed the corresponding data. Wei XIONG wrote the first draft of the manuscript. Wei XIONG, Qi-min ZHANG, and Jian-feng WANG revised and edited the final version.

Conflict of interest

Wei XIONG, Qi-min ZHANG, and Jian-feng WANG declare that they have no conflict of interest.

References

Alikarami R, Andò E, Gkiousas-Kapnisis M, et al., 2015. Strain localisation and grain breakage in sand under shearing at high mean stress: insights from in situ X-ray tomography. *Acta Geotechnica*, 10(1):15-30. https://doi.org/10.1007/s11440-014-0364-6

Altuhafi FN, Coop MR, 2011. Changes to particle characteristics associated with the compression of sands. *Géotechnique*, 61(6):459-471. https://doi.org/10.1680/geot.9.P.114

Andrade JE, Avila CF, Hall SA, et al., 2011. Multiscale modeling and characterization of granular matter: from grain kinematics to continuum mechanics. *Journal of the Mechanics and Physics of Solids*, 59(2):237-250. https://doi.org/10.1016/j.jmps.2010.10.009

Azéma E, Radjai F, Dubois F, 2013. Packings of irregular polyhedral particles: strength, structure, and effects of angularity. *Physical Review E*, 87(6):062203. https://doi.org/10.1103/PhysRevE.87.062203

Bao N, Wei J, Chen JF, et al., 2020. 2D and 3D discrete numerical modelling of soil arching. *Journal of Zhejiang University-SCIENCE A (Applied Physics & Engineering)*, 21:350-365. https://doi.org/10.1631/jzus.A1900672

Chen RC, Dreossi D, Mancini L, et al., 2012. PITRE: software for phase-sensitive X-ray image processing and tomography reconstruction. *Journal of Synchrotron Radiation*, 19(5):836-845. https://doi.org/10.1107/S0909049512029731

Cheng Z, Wang JF, 2018a. Experimental investigation of interparticle contact evolution of sheared granular materials using X-ray micro-tomography. *Soils and Foundations*, 58(6):1492-1510. https://doi.org/10.1016/j.sandf.2018.08.008

Cheng Z, Wang JF, 2018b. A particle-tracking method for experimental investigation of kinematics of sand particles under triaxial compression. *Powder Technology*, 328: 436-451. https://doi.org/10.1016/j.powtec.2017.12.071

Cheng Z, Wang JF, Coop MR, et al., 2020a. A miniature triaxial apparatus for investigating the micromechanics of granular soils with in situ X-ray micro-tomography scanning. *Frontiers of Structural and Civil Engineering*, 14(2):357-373. https://doi.org/10.1007/s11709-019-0599-2

Cheng Z, Zhou B, Wang JF, 2020b. Tracking particles in sands based on particle shape parameters. *Advanced Powder Technology*, 31(5):2005-2019. https://doi.org/10.1016/j.apt.2020.02.033

Cho GC, Dodds J, Santamarina JC, 2006. Particle shape effects on packing density, stiffness, and strength: natural and crushed sands. *Journal of Geotechnical and Geoenvironmental Engineering*, 132(5):591-602. https://doi.org/10.1061/(ASCE)1090-0241(2006)132:5(591)

Cundall PA, Strack ODL, 1979. A discrete numerical model for granular assemblies. *Géotechnique*, 29(1):47-65. https://doi.org/10.1680/geot.1979.29.1.47

de Bono JP, McDowell GR, 2014. DEM of triaxial tests on crushable sand. *Granular Matter*, 16(4):551-562. https://doi.org/10.1007/s10035-014-0500-x

de Bono JP, McDowell GR, 2020. The effects of particle shape on the yielding behaviour of crushable sand. *Soils and Foundations*, 60(2):520-532. https://doi.org/10.1016/j.sandf.2020.04.001

de Bono JP, McDowell GR, Wanatowski D, 2012. Discrete element modelling of a flexible membrane for triaxial testing of granular material at high pressures. *Géotechnique Letters*, 2(4):199-203. https://doi.org/10.1680/geolett.12.00040

Fazekas S, Török J, Kertész J, et al., 2006. Morphologies of three-dimensional shear bands in granular media. *Physical Review E*, 74(3):031303. https://doi.org/10.1103/PhysRevE.74.031303

Fei WB, Narsilio GA, 2020. Impact of three-dimensional sphericity and roundness on coordination number. *Journal of Geotechnical and Geoenvironmental Engineering*, 146(12):06020025. https://doi.org/10.1061/(asce)GT.1943-5606.0002389

Fonseca J, O'Sullivan C, Coop MR, et al., 2012. Non-invasive characterization of particle morphology of natural sands. *Soils and Foundations*, 52(4):712-722. https://doi.org/10.1016/j.sandf.2012.07.011

Fonseca J, O'Sullivan C, Coop MR, et al., 2013. Quantifying the evolution of soil fabric during shearing using directional parameters. *Géotechnique*, 63(6):487-499. https://doi.org/10.1680/geot.12.P.003

Gong J, Liu J, 2017. Effect of aspect ratio on triaxial compression of multi-sphere ellipsoid assemblies simulated using a discrete element method. *Particuology*, 32:49-62. https://doi.org/10.1016/j.partic.2016.07.007

Grigoriu M, Garboczi E, Kafali C, 2006. Spherical harmonic-based random fields for aggregates used in concrete. *Powder Technology*, 166(3):123-138. https://doi.org/10.1016/j.powtec.2006.03.026

Gutierrez M, Wang J, Yoshimine M, 2009. Modeling of the simple shear deformation of sand: effects of principal stress rotation. *Acta Geotechnica*, 4(3):193-201. https://doi.org/10.1007/s11440-009-0094-3

Hall SA, Bornert M, Desrues J, et al., 2010. Discrete and continuum analysis of localised deformation in sand using X-ray μCT and volumetric digital image correlation. *Géotechnique*, 60(5):315-322. https://doi.org/10.1680/geot.2010.60.5.315

Hasan A, Alshibli KA, 2010. Experimental assessment of 3D particle-to-particle interaction within sheared sand using synchrotron microtomography. *Géotechnique*, 60(5):369-379. https://doi.org/10.1680/geot.2010.60.5.369

Huang ZY, Yang ZX, Wang ZY, 2008. Discrete element modeling of sand behavior in a biaxial shear test. *Journal of Zhejiang University-SCIENCE A*, 9(9):1176-1183. https://doi.org/10.1631/jzus.A0720059

Iwashita K, Oda M, 2000. Micro-deformation mechanism of shear banding process based on modified distinct element method. *Powder Technology*, 109(1-3):192-205. https://doi.org/10.1016/S0032-5910(99)00236-3

Jin Z, Lu Z, Yang Y, 2021. Numerical analysis of column collapse by smoothed particle hydrodynamics with an advanced critical state-based model. *Journal of Zhejiang University-SCIENCE A (Applied Physics & Engineering)*, 22(11):882-893. https://doi.org/10.1631/jzus.A2000598

Karatza Z, Andò E, Papanicolopulos SA, et al., 2018. Evolution of deformation and breakage in sand studied using X-ray tomography. *Géotechnique*, 68(2):107-117. https://doi.org/10.1680/jgeot.16.P.208

Kawamoto R, Andò E, Viggiani G, et al., 2018. All you need is shape: predicting shear banding in sand with LS-DEM. *Journal of the Mechanics and Physics of Solids*, 111:375-392. https://doi.org/10.1016/j.jmps.2017.10.003

Kuhn MR, Sun W, Wang Q, 2015. Stress-induced anisotropy in granular materials: fabric, stiffness, and permeability. *Acta Geotechnica*, 10(4):399-419. https://doi.org/10.1007/s11440-015-0397-5

Lin X, Ng TT, 1997. A three-dimensional discrete element model using arrays of ellipsoids. *Géotechnique*, 47(2):319-329. https://doi.org/10.1680/geot.1997.47.2.319

Liu X, Garboczi EJ, Grigoriu M, et al., 2011. Spherical harmonic-based random fields based on real particle 3D data: improved numerical algorithm and quantitative comparison to real particles. *Powder Technology*, 207(1-3):78-86. https://doi.org/10.1016/j.powtec.2010.10.012

Maeda K, Sakai H, Kondo A, et al., 2010. Stress-chain based micromechanics of sand with grain shape effect. *Granular Matter*, 12(5):499-505. https://doi.org/10.1007/s10035-010-0208-5

Mollon G, Zhao JD, 2014. 3D generation of realistic granular samples based on random fields theory and fourier shape descriptors. *Computer Methods in Applied Mechanics and Engineering*, 279:46-65. https://doi.org/10.1016/j.cma.2014.06.022

Nassauer B, Liedke T, Kuna M, 2013. Polyhedral particles for the discrete element method. *Granular Matter*, 15(1):85-93. https://doi.org/10.1007/s10035-012-0381-9

Ng TT, 2009. Particle shape effect on macro- and micro-behaviors of monodisperse ellipsoids. *International Journal for Numerical and Analytical Methods in Geomechanics*, 33(4):511-527. https://doi.org/10.1002/nag.732

Nie JY, Cao ZJ, Li DQ, et al., 2021. 3D DEM insights into the effect of particle overall regularity on macro and micro mechanical behaviours of dense sands. *Computers and Geotechnics*, 132:103965. https://doi.org/10.1016/j.compgeo.2020.103965

Nie ZH, Fang CF, Gong J, et al., 2020. DEM study on the effect of roundness on the shear behaviour of granular materials. *Computers and Geotechnics*, 121:103457. https://doi.org/10.1016/j.compgeo.2020.103457

Otsu N, 1979. A threshold selection method from gray-level histograms. *IEEE Transactions on Systems, Man, and Cybernetics*, 9(1):62-66. https://doi.org/10.1109/TSMC.1979.4310076

Perona P, Malik J, 1990. Scale-space and edge detection using anisotropic diffusion. *IEEE Transactions on Pattern Analysis and Machine Intelligence*, 12(7):629-639. https://doi.org/10.1109/34.56205

Qu TM, Feng YT, Wang Y, et al., 2019. Discrete element modelling of flexible membrane boundaries for triaxial tests. *Computers and Geotechnics*, 115:103154. https://doi.org/10.1016/j.compgeo.2019.103154

Qu TM, Wang M, Feng YT, 2022. Applicability of discrete element method with spherical and clumped particles for constitutive study of granular materials. *Journal of Rock Mechanics and Geotechnical Engineering*, 14(1):240-251. https://doi.org/10.1016/j.jrmge.2021.09.015

Rothenburg L, Bathurst RJ, 1991. Numerical simulation of idealized granular assemblies with plane elliptical particles. *Computers and Geotechnics*, 11(4):315-329. https://doi.org/10.1016/0266-352X(91)90015-8

Sharma A, Leib-Day AR, Thakur MM, et al., 2021. Effect of particle morphology on stiffness, strength and volumetric behavior of rounded and angular natural sand. *Materials*, 14(11):3023. https://doi.org/10.3390/ma14113023

Stroeven P, He H, Stroeven M, 2011. Discrete element modelling approach to assessment of granular properties in concrete. *Journal of Zhejiang University-SCIENCE A (Applied Physics & Engineering)*, 12(5):335-344. https://doi.org/10.1631/jzus.A1000223

Sun Q, Zheng JX, 2021. Realistic soil particle generation based on limited morphological information by probability-based spherical harmonics. *Computational Particle Mechanics*, 8(2):215-235. https://doi.org/10.1007/s40571-020-00325-6

Thakur MM, Penumadu D, 2021. Influence of friction and particle morphology on triaxial shearing of granular materials. *Journal of Geotechnical and Geoenvironmental Engineering*, 147(11):04021118. https://doi.org/10.1061/(asce)GT.1943-5606.0002634

Viggiani G, Andò E, Takano D, et al., 2015. Laboratory X-ray tomography: a valuable experimental tool for revealing processes in soils. *Geotechnical Testing Journal*, 38(1):61-71. https://doi.org/10.1520/GTJ20140060

Wang JF, Yan HB, 2012. DEM analysis of energy dissipation in crushable soils. *Soils and Foundations*, 52(4):644-657. https://doi.org/10.1016/j.sandf.2012.07.006

Wang X, Yin ZY, Su D, et al., 2022. A novel approach of random packing generation of complex-shaped 3D particles with controllable sizes and shapes. *Acta Geotechnica*, 17(2):355-376. https://doi.org/10.1007/s11440-021-01155-3

Wei DH, Wang JF, Nie JY, et al., 2018. Generation of realistic sand particles with fractal nature using an improved spherical harmonic analysis. *Computers and Geotechnics*, 104:1-12. https://doi.org/10.1016/j.compgeo.2018.08.002

Wen MJ, Wang KH, Wu WB, et al., 2021. Dynamic response

of bilayered saturated porous media based on fractional thermoelastic theory. *Journal of Zhejiang University-SCIENCE A (Applied Physics & Engineering)*, 22: 992-1004.
https://doi.org/10.1631/jzus.A2100084

Wu MM, Wang JF, Russell A, et al., 2021. DEM modelling of mini-triaxial test based on one-to-one mapping of sand particles. *Géotechnique*, 71(8):714-727.
https://doi.org/10.1680/jgeot.19.P.212

Wu ZJ, Li ZL, Huang WD, et al., 2012. Comparisons of nozzle orifice processing methods using synchrotron X-ray micro-tomography. *Journal of Zhejiang University-SCIENCE A (Applied Physics & Engineering)*, 13(3): 182-188.
https://doi.org/10.1631/jzus.A1100252

Xiao Y, Long LH, Matthew Evans T, et al., 2019. Effect of particle shape on stress-dilatancy responses of medium-dense sands. *Journal of Geotechnical and Geoenvironmental Engineering*, 145(2):04018105.
https://doi.org/10.1061/asce)GT.1943-5606.0001994

Xiong W, Wang JF, 2021. Gene mutation of particle morphology through spherical harmonic-based principal component analysis. *Powder Technology*, 386:176-192.
https://doi.org/10.1016/j.powtec.2021.03.032

Xiong W, Wang JF, Cheng Z, 2020. A novel multi-scale particle morphology descriptor with the application of SPHERICAL harmonics. *Materials*, 13(15):3286.
https://doi.org/10.3390/ma13153286

Yang J, Luo XD, 2015. Exploring the relationship between critical state and particle shape for granular materials. *Journal of the Mechanics and Physics of Solids*, 84:196-213.
https://doi.org/10.1016/j.jmps.2015.08.001

Yin ZY, Jin YF, Zhang X, 2021. Large deformation analysis in geohazards and geotechnics. *Journal of Zhejiang University-SCIENCE A (Applied Physics & Engineering)*, 22:851-855.
https://doi.org/10.1631/jzus.A21LDGG1

Zhang WC, Wang JF, Jiang MJ, 2013. DEM-aided discovery of the relationship between energy dissipation and shear band formation considering the effects of particle rolling resistance. *Journal of Geotechnical and Geoenvironmental Engineering*, 139(9):1512-1527.
https://doi.org/10.1061/(asce)GT.1943-5606.0000890

Zhao B, Wang J, Coop MR, et al., 2015. An investigation of single sand particle fracture using X-ray micro-tomography. *Géotechnique*, 65(8):625-641.
https://doi.org/10.1680/geot.4.P.157

Zhao BD, Wang JF, 2016. 3D quantitative shape analysis on form, roundness, and compactness with μCT. *Powder Technology*, 291:262-275.
https://doi.org/10.1016/j.powtec.2015.12.029

Zhao BD, Wang JF, Andò E, et al., 2020. Investigation of particle breakage under one-dimensional compression of sand using X-ray microtomography. *Canadian Geotechnical Journal*, 57(5):754-762.
https://doi.org/10.1139/cgj-2018-0548

Zheng J, Hryciw RD, 2017. Soil particle size and shape distributions by stereophotography and image analysis. *Geotechnical Testing Journal*, 40(2):317-328.
https://doi.org/10.1520/GTJ20160165

Zhou B, Wang J, 2017. Generation of a realistic 3D sand assembly using X-ray micro-computed tomography and spherical harmonic-based principal component analysis. *International Journal for Numerical and Analytical Methods in Geomechanics*, 41(1):93-109.
https://doi.org/10.1002/nag.2548

Zhou B, Huang RQ, Wang HB, et al., 2013. DEM investigation of particle anti-rotation effects on the micromechanical response of granular materials. *Granular Matter*, 15(3): 315-326.
https://doi.org/10.1007/s10035-013-0409-9

Zhou B, Wang JF, Zhao BD, 2015. Micromorphology characterization and reconstruction of sand particles using micro X-ray tomography and spherical harmonics. *Engineering Geology*, 184:126-137.
https://doi.org/10.1016/j.enggeo.2014.11.009

Zhou B, Wang J, Wang H, 2018. A novel particle tracking method for granular sands based on spherical harmonic rotational invariants. *Géotechnique*, 68(12):1116-1123.
https://doi.org/10.1680/jgeot.17.T.040

Electronic supplementary materials

Table S1